

CIRCULATION COPY

UCID-20264

**SUBJECT TO RECALL
IN TWO WEEKS**

**SURVEY OF INITIAL EXPERIMENTS
ON ATA BEAM DYNAMICS**

**D. S. Prono, G. J. Caporaso, Y. P. Chong,
T. J. Fessenden, R. E. Hester, E. J. Lauer,
T. J. Orzechowski, A. C. Paul, J. T. Weir**

June 25, 1984

**Lawrence
Livermore
National
Laboratory**

This is an informal report intended primarily for internal or limited external distribution. The opinions and conclusions stated are those of the author and may or may not be those of the Laboratory.

DISCLAIMER

This document was prepared as an account of work sponsored by an agency of the United States Government. Neither the United States Government nor the University of California nor any of their employees, makes any warranty, express or implied, or assumes any legal liability or responsibility for the accuracy, completeness, or usefulness of any information, apparatus, product, or process disclosed, or represents that its use would not infringe privately owned rights. Reference herein to any specific commercial products, process, or service by trade name, trademark, manufacturer, or otherwise, does not necessarily constitute or imply its endorsement, recommendation, or favoring by the United States Government or the University of California. The views and opinions of authors expressed herein do not necessarily state or reflect those of the United States Government or the University of California, and shall not be used for advertising or product endorsement purposes.

Printed in the United States of America
Available from
National Technical Information Service
U.S. Department of Commerce
5285 Port Royal Road
Springfield, VA 22161
Price: Printed Copy \$; Microfiche \$4.50

Page Range	Domestic Price	Page Range	Domestic Price
001-023	\$ 7.00	326-350	\$ 26.50
026-050	8.50	351-375	28.00
051-075	10.00	376-400	29.50
076-100	11.50	401-426	31.00
101-125	13.00	427-450	32.50
126-150	14.50	451-475	34.00
151-175	16.00	476-500	35.50
176-200	17.50	501-525	37.00
201-225	19.00	526-550	38.50
226-250	20.50	551-575	40.00
251-275	22.00	576-600	41.50
276-300	23.50	601-625	
301-325	25.00		

Add 1.50 for each additional page beyond 625 pages.
Current price of paper not

SURVEY OF INITIAL EXPERIMENTS ON ATA BEAM DYNAMICS

**D. S. Prono, G. J. Caporaso, Y. P. Chong, T. J. Fessenden,
R. E. Hester, E. J. Lauer, T. J. Orzechowski, A. C. Paul, J. T. Weir**

**Lawrence Livermore National Laboratory
University of California
Livermore, California 94550**

June 25, 1984

ABSTRACT

The Advanced Test Accelerator (ATA) is a linear induction electron accelerator whose design parameters are 50 MeV, 10 kA and 70 ns pulse duration. The key physics issues affecting performance of the accelerator involve beam dynamics during transport through the accelerator structure. In this report, we present experimental results describing the initial operating phases of ATA. These results illustrate the complexity of the beam transport phenomena but also indicate the means to stabilize beam dynamics. Improvements in beam transport which result from deploying various stabilization techniques are also presented.

Work performed jointly under the auspices of the U. S. Department of Energy by Lawrence Livermore National Laboratory under Contract W-7405-ENG-48 and for the Department of Defense under Defense Advanced Research Projects Agency ARPA Order No. 4395 Amendment No. 31, monitored by Naval Surface Weapons Center under document number N60921-84-W0080.

INTRODUCTION

The Advanced Test Accelerator is a linear induction electron accelerator which is configured as follows. The electron beam is created in the injector which nominally produces a 10 kA, 2.5 MeV, 70 ns pulse. The operating performance and characteristics of this injector have been described in a previous report.¹ Immediately upon being accelerated to 2.5 MeV, the beam enters a continuous solenoidal transport system. The axial magnetic field is varied over the first four meters of transport so that the beam is gradually focused down from an initial ~12.5 cm radius to ~2 cm radius. At this point, the beam enters a series of accelerating cavities. A cross-section of one such accelerating cavity is shown in Figure 1. As shown in Figure 1, each accelerating cavity has its own solenoid capable of 3 kG fields. These cavities are induction accelerator cores which operate on the principle of an auto transformer. An input primary power pulse of 250 kV is fed into the cavity and completes a high impedance inductive loop. The cavity is configured such that the full potential drop across this inductive loop also appears across the accelerator gap. In passing through this accelerator gap, the electron beam and its image wall return current complete a secondary current loop which inductively couples to the primary power circuit. In this manner, the kinetic energy of the electron beam is increased by the full 250 kV potential of the single accelerating core. In Figure 2, we indicate the equivalent circuit of an accelerating core. Note that the beam is represented as a constant current source; this implies that the time variation of the cavity's magnetic fields induced by the beam loads the cavity and alters the accelerating potential. This condition ultimately couples back to

the beam and influences beam dynamics. Also, note that the accelerating gap of each cavity (see Figure 1) necessarily forms a discontinuity in the vacuum transport. At each such break in the circular cross-section boundary, there is no longer a balance of electric and magnetic fields (the radial electric field is slightly distorted but the azimuthal magnetic field is no longer bounded). This localized imbalance of the beam's magnetic and electric fields also affects beam transport.

The first thirty accelerating cavities are assembled in six modules, each of which has five cavities alternately spaced by a solenoidal magnet. Since the beam energy in this beginning portion of the accelerator is low, the confining axial magnetic field is held to values well below the limits set by virtual cathode formation. Since the beam breakup instability and image displacement instabilities are accentuated in transport regions of high gap density and low magnetic fields, the initial portion of the accelerator has the wide spacing between accelerator gaps (alternating with solenoids) in order to gradually and smoothly increase the axial field and beam energy. Beyond this point (beam energy greater than 10 MeV), the remaining 160 accelerator cavities are configured into 16 modules of ten cavities directly adjoining each other. Such a 10-cavity module is shown in Figure 3. For these modules, the magnetic field is usually set at a uniform high value of ~3 kG. This field uniformity is allowed for beam energies greater than ~10 MeV since the beam is emittance dominated. Consequently, the space charge component of the beam envelope equation can be ignored and the γ independent beam equilibrium radius is only dependent on source emittance and axial magnetic field.

Between each 5 or 10 cavity module is a vacuum pumping station. Discrete solenoids form the section of the transport thereby making the axial magnetic field nearly continuous. This section of transport is also equipped with an x-y steering coil set and a diagnostic unit. The standard diagnostic unit is a resistive current monitor (giving total current and two-dimensional centroid measurements), an array of B_{θ} -rf loops (giving a signal proportional to $\frac{d}{dt} (I/R)$ and also recording the rf noise spectrum of the beam), an x-ray plunging probe (which yields a radial beam density profile by scanning a small high Z target radially across the beam). These three measurements techniques are used the entire length of ATA and form the core accelerator diagnostics. Additional measurements which also help characterize accelerator performance are:

- i) gated TV's viewing beam intercept foils which also indicate beam profile;
- ii) beam emittance and beam energy measurement techniques;
- iii) determination of the magnetic profile through the entire accelerator, both axial field strength and x-y steering coil strength.

FIRST EXPERIMENTAL OBSERVATIONS

Initial experiments with the ATA involved accelerating the beam through the first six accelerator modules (five accelerator cavities per module) to an energy of 10 MeV. Sample data from these initial experiments are shown in Figures 4a and 4b. For these initial experiments, steering coils were not yet operational. Consequently, no corrections could be made to maintain the beam

centroid on axis. Data shown in Figure 4a show the 7 kA beam current at entrance to the accelerator modules; the beam centroid is slightly (~ 3 mm) off axis. By the 10 MeV location, the relatively quiescent input beam current profile had become distorted by the appearance of large notches and spikes. The offset of beam centroid had grown significantly to ~ 1.1 cm accompanied by large spatial oscillations at the beginning and end of the beam current pulse (time of maximum dI/dt). Monitors of x-ray emission from the accelerator wall showed spikes of current intercepting the accelerator vacuum wall. The \dot{B}_θ -probes located along the accelerator show a progressive increase in beam offset during the time of high \dot{B}_θ with a characteristic frequency increasing the further the beam is transported. Also apparent in the most downstream rf loop is the ~ 800 MHz oscillation characteristic of the beam breakup (BBU) cavity-interaction mode. Since the \dot{B}_θ probe senses $\frac{d}{dt} (I/R)$, the indicated amplitude of the spatial oscillations is weighted by the oscillation frequency; thus the lower frequency motion of the beam head and tail is far more severe than the BBU oscillations.

The lower frequency disruptions of the beam pulse clearly represent unwanted beam dynamics adversely affecting beam transport. Minimizing these oscillations occurs when the beam rise time is sharply decreased. Data shown in Figure 5a show that a current pulse with a times 6 slower rise time ($dI/dt \sim 1.3 \times 10^{11}$ A/sec, compared to previous $dI/dt \sim 8 \times 10^{11}$ A/sec) is accelerated to 10 MeV with minimum pulse disruption. However, the end of the beam pulse still has a high dI/dt and pulse disruption is apparent on the oscilloscope traces showing beam current, beam centroid, and \dot{B}_θ . We note that the slow I beam still develops centroid offset (again, no compensating

steering coils were used). Although the beginning of the beam is relatively centered on axis but that the end of the beam pulse, immediately preceding the fast \dot{I} turn-off, is offset. As previously mentioned, the beam current inductively loads the accelerating cavities during the pulse rise and fall time. Shown in Figure 5b are traces of an accelerator cavity voltage when the beam current has a fast and slow rate of rise. Loading due to the fast \dot{I} clearly induces a \dot{V} on the time changing beam.

Explanation of these initial observations includes two phenomena. First, at low energy, the beam axial magnetic transport system is dominated by the balance of magnetic field and space charge forces. If the magnetic field is set to have the peak current in radial equilibrium, then inevitably the current rise and fall is "mismatched" resulting in radial oscillations. Figure 6 shows computations of the beam envelope new match for a 10 kA, 2.5 MeV beam leaving the ATA injector, being transported through and accelerated by the first two five-cavity modules. The z-axial magnetic field increases from 200 G to 2 kG and the beam gains 250 keV at each designated accelerator gap. The 10 kA beam has a relatively smooth envelope indicating that the magnetic field variation is well "matched." However, the lower current values indicate that the beam beginning and end is "mismatched" and radial oscillations of the beam envelope result. This phenomenon may partially explain some of the current loss (wall x-ray signals) and degradation of the rising and falling portions of the transported beam current.

The second mechanism affecting beam motion is referred to as beam corkscrew dynamics². This phenomenon simply involves the normal helical motion of an offset beam propagating off axis in an axial magnetic field, with the added complication of there being a slight sinusoidal energy variation.

For a beam with initial conditions at $z = 0$ of $x = 2x_0$, $\frac{dx}{dz} = Kx_0$, and $y = \frac{dy}{dz} = 0$, the equations of motion are simply sinusoidal in kZ . However, if there is a temporal energy variation, (i.e., $\gamma = \gamma_0(1 + \frac{\Delta\gamma}{\gamma_0} \sin \omega\tau)$), then the equations of motion are a summation of harmonics in ω . The amplitude of the N th harmonic is approximately $2 x_0 \left(\frac{K_0 Z}{2} \frac{\Delta\gamma}{\gamma} \right)^n$, so that the uniform offset equal to $2x_0$ becomes a time-varying displacement of amplitude growing asymptotically to a value of $2x_0$ and with the frequency upshifting for greater transport lengths Z . This model explains why the fast \dot{I} beam with the sinusoidal-like loading of the accelerator cavity voltage has a disruptive beam transport characteristic. The frequency upshift is clearly apparent in the data and closer examination of selected traces of x - y beam centroid motion does indicate (see Figure 7) beam helical precession.

In subsequent experiments with beam acceleration and transport through to 10 MeV, deployment of steering coils gave us the capability of maintaining beam centroid on axis and of developing greater finesse in tuning the accelerator—both in terms of the setting of the axial magnetic field for better matching and also in injector operational characteristics. Figure 8 shows measurements of beam current and centroid movement at the injector output and at the 10 MeV accelerator location. There is obvious improvement in performance, but the disruptive beam dynamics have only been reduced, not eliminated. During these experiments, we observed that relatively subtle changes in injector operation did affect beam dynamics. The waveforms shown in Figure 9 indicate the sensitivity of the total transmitted current at the 10 MeV location to settings of the injector's bucking coil¹ and the cathode ignitor timing. The changes in injector operation did not produce any

observable change in macroscopic beam characteristics (I, \hat{x}, \hat{y}) as the beam emerged from the injector. However, after beam transport through six five-cell accelerator modules, these same macroscopic observables showed the appearance of disruptive beam dynamics that were controllable by injector operating conditions. These subjective observations indicate that microstructure of the injector output beam contributes to transverse centroid fluctuations.

Data from x-ray plunging probes determine the radial profile of the beam current density within the accelerator. Such data are shown in Figure 10. These data indicate a temporal variation of the radial distribution of beam density during the beam pulse as well as asymmetric wings to the beam profile. Although the beam density in the wings is low when weighted by R^2 , the total amount of current carried in the asymmetric wings is not small (up to ~30% of the total beam current). The presence of these wings indicates that the injector beam output has a class of particles whose orbits undergo large radial excursions.

Recognizing the asymmetry of the wings in the beam profile, we deployed a collimator between the injector and first accelerator module. This collimator was 4 cm diameter and was 1.06 meters long. The axial magnetic field through the collimator was held at ~1 kG. This collimator obviously bounded phase space of the beam (i.e., was an emittance filter). The beam that passed through the collimator entered the accelerator with its centroid well behaved ($x = y = \frac{dx}{dz} = \frac{dy}{dz} = 0$). The maximum "filtered current through the collimator always was 3 to 3.5 kA independent of the injector output current which varied from 4 to 8 kA. The filtered current pulse was sufficiently well behaved such that it could be accelerated to 20 MeV (through six five-cell accelerator

modules and four ten-cell modules). The data of Figure 11 show how the collimator limits transmitted current and sharpens pulse rise time (eclipses the mismatched low-current which undergo radial pulsations). The remaining data indicate that total current, centroid motion, and \dot{B}_z of the beam at 20 MeV are minimally distorted by the low frequency, disruptive beam dynamics.

The collimated beam experiments suggest that the injector's output beam has a class of particles capable of executing large radial excursions into regions of bad (highly scalloped) magnetic field. The loss of such particles to the vacuum wall would cause abrupt centroid displacements. Eliminating these particles before they enter the accelerator structure and ensuring that the beam is properly directed ($x = y = \frac{dx}{dz} = \frac{dy}{dz} = 0$) then allows the beam centroid to be maintained on axis, thereby limiting the onset of transverse motion that leads to disruptive beam dynamics. With a collimated beam, the dynamics of the beam transport through the entire accelerator was studied. Figure 12 shows samples of beam current, centroid and \dot{B}_z characteristics of the beam at the end of the accelerator. For these conditions, the collimated beam was accelerated and transported through all cavities. One group of data shows beam characteristics resulting from using the 4 cm diameter collimator. "Corkscrewing" at the beam rise and fall are still apparent but the central high current portion of the beam body is stable. Also, for this condition there is no current loss through the accelerator. The second data group resulted from using a 6 cm diameter collimator. For this larger collimator, the degradation in beam dynamics throughout the entire pulse is clearly apparent with a current loss distributed throughout the accelerator. This behavior further suggests that a fraction of the total injector output pulse undergoes poor transport optics.

With a collimated beam, more controlled experiments could be performed. The aim of these experiments was to investigate other possible causes of unwanted beam motion and current loss. Our conclusions from these are as follows:

- i) that beam dynamics were not caused by pulse power drive asymmetries;
- ii) that the beam dynamics were not caused by collective effects (current dependence was weak if at all important);
- iii) and that transverse field errors of the accelerator solenoids were small and within tolerance. However, even small transverse field errors can cause offsets of the beam centroid. Consequently, we are minimizing all possible sources of field asymmetries.

During the course of these experiments, we found why the steering coils exhibited far weaker control of the beam than anticipated. These steering coils were located over the current monitors which housed an annular ring of ferrite that effectively shorted out approximately 40% of the steering coils transverse field. Correcting this situation requires moving the steering coils to locations free of ferrite material.

A final experimental arrangement was used to further investigate the sources of transverse beam dynamics. With no collimator between the injector and the accelerator, a "wire-zone" was installed in place of the third five-cell module. Immediately beyond the wire zone was a 5 cm thick variable beam attenuator which had open-spaced transparencies ranging from 10% to 100%. The detailed operation of a wire zone has been reported elsewhere.³ A beam exiting a wire zone, just as beam exiting a collimator, has its centroid characteristics being $x = y = \frac{dx}{dz} = \frac{dy}{dz} = 0$. However, a wire zone centers the beam without a loss of current and without bounding phase

space (no limitation on emittance or particles capable of far off-axis orbits). These experiments, summarized in Figure 13, indicate that after the wire zone, and regardless of the magnitude of beam current set by the variable attenuator, there is distributed current loss through the remainder of the accelerator even though the centroid motion is less than one centimeter. The results again indicate the presence of a class of beam particles from the injector that are capable of large radial orbits. The wire zone "passes" these particles but the collimator stops them. Beam transverse fluctuations on the head and tail of the pulse still occur consistent with the corkscrew mode. Development of transverse displacement within the central portion of the beam pulse is either caused by small transverse field errors or by asymmetric current loss which causes transverse centroid motion.

SUMMARY AND CONCLUSIONS

Initial operation of ATA has demonstrated the integrity of the accelerator and its pulsed power system. Low frequency transverse fluctuations in the beam centroid have restricted the beam current to approximately 7 kA. These dynamics result from small centroid offsets being frequency upshifted due to a slight energy variation in the beam and the effect of that variation on the normal helical motion within a solenoidal field. To avoid these deleterious beam dynamics requires continual centering of the centroid (the energy variation can be corrected but the expense of necessary power supply modifications is prohibitive). The centroid displacements are not driven by pulsed power asymmetries and do not appear to be a collective (current dependent) phenomenon. The influence of image

displacement effects (beam centroid passing through a gap off-axis thereby having an imbalance of magnetic and electric images) has been observed, but the resultant period of these perturbations is very long and correctable by proper use of the steering coils. However, the localized loss of large orbiting beam particles that populate the asymmetric wings of the beam profile causes discrete shifts in the centroid which can initiate degradation in beam transport. Using a collimator which absorbs the particles capable of large radial orbits clearly minimizes transverse fluctuations of the beam centroid and results in improved beam transport. Research is presently in progress to make a high current beam injector which does not produce particles capable of the large radial excursions. Our approach is to use high field gradient field emission cathodes with a of small area (high current density) and without a control grid. Such an injector-cathode arrangement would avoid both the marginally dense plasma that is characteristic of the present plasma surface discharge cathode and plasma-grid interaction which creates an unwanted current source.¹ Both of these phenomena may contribute to the production of beam particles that exhibit high effective emittance and large radial orbits.

REFERENCES

1. D. S. Prono, D. L. Bix, R. J. Briggs, Y. P. Chong, T. J. Fessenden, R. E. Hester, E. J. Lauer, T. J. Orzechowski, and K. W. Struve, First Studies of ATA Injector, August 1, 1983, Lawrence Livermore National Laboratory, UCID-19862.
2. G. L. Caporaso, et al., Beam Dynamics in the Advanced Test Accelerator (ATA), September 28, 1983, Lawrence Livermore National Laboratory, UCRL-89881.
3. D. S. Prono, et al., Electron Beam Guiding and Phase Mix Damping by an Electrostatically Charged Wire, Physical Review Letters, Volume 51, Number 9, 29 August 1983, p. 723.

FIGURE CAPTIONS

Fig. 1. Cross section of a single accelerator cavity. Shown are the a) power input feed, b) ferrite which increases the load impedance of the shorted turn inductive lap and adds volt-seconds, c) the vacuum 250 kV accelerator gap, d) the oil-to-vacuum insulator, e) corner reflector and mode damping ferrite which minimize higher order cavity modes, f) solenoid.

Fig. 2. Equivalent circuit of pulsed power drive and accelerator core. The electron beam load is a constant current source, the input power source from a blumlein feeding a transmission line is modeled as a constant impedance voltage source and the very high impedance cavity inductance which is resistively shunted to match to the transmission line is simply modeled as the resistive load.

Fig. 3. Shown is an assembled 10-cavity module; the cut-away section exposes the accelerating cavity and the encased solenoid.

Fig. 4a. Shown are oscilloscope traces of beam current and beam centroid position in the horizontal and vertical plane. Centroid location is given by the relation $x(t), y(t) = V_{x,y}(t) \times R/2 V_I(t)$ where R = vacuum pipe radius 6.7 cm, $V_I(t)$ is the time dependent total current voltage signal, and $V_{x,y}(t)$ is the time dependent centroid voltage signal. The two sets of data show the input beam conditions and exit beam conditions after acceleration by and transport through the first thirty accelerator cavities. The x-ray monitoring photomultiplier shows bursts of x-rays caused by spikes of beam current intercepting the vacuum wall.

Fig. 4b. Shown are oscilloscope traces of the beam's \dot{B}_θ signal ($= \frac{d}{dt} I/R$) at various locations progressively along the accelerator. Note the signature of the corkscrew mode on the beam head (increasing frequency with propagation distance) and the eventual appearance of the 800 MHz BBU oscillations.

Fig. 5a. Oscilloscope traces of accelerator performance through 10 MeV showing total current and beam centroid motion for operating conditions of a much slower beam current rise time. Note that beam centroid shows offset but no axis-crossing beam sweep.

Fig. 5b. Data showing how varying the beam current rise time affects the accelerator cavity voltage.

Fig. 6. Computations of the beam envelope equation for the first 8 meters of transport using various values of injector output beam current being transported through (while being accelerated) a realistic axial magnetic field that is matched (causing minimum radial pulsations) for high currents. As shown, lower currents (during beam rise and fall) are mismatched and experience serious radial oscillations of the beam envelope.

Fig. 7. Oscilloscope traces showing details of beam centroid motion in the x and y planes for the rising current portion of a beam pulse. The phasing of the transverse motion in the orthogonal planes is consistent with helical beam motion.

Fig. 8. Data of beam characteristics showing beam current and x-y centroid motion at the beginning of the accelerator and at the 10 MeV location. The improved performance resulted from using steering coils to maintain beam centroid on axis and from improved operation of the injector.

Fig. 9. For slight adjustments in injector operations (as shown: top-bucking coil on/off and bottom-ignitor timing 80 ns/60 ns) there is significant change in beam properties by the 10 MeV location. For these different operating conditions, there is no discernible change in injector output beam macroscopic observables $I(t)$, $\hat{x}(t)$ and $\hat{y}(t)$; this suggests that beam micro structure is influential in beam dynamics.

Fig. 10. Data showing radial dependence of plunging x-ray probe signal which is proportional to the current density. The time varying asymmetric wings indicate that the injector output has a time-dependent class of particles that is capable of large radial motion.

Fig. 11. Data of beam characteristics (beam current, $I(t)$; beam centroid motion, $\hat{x}(t)$, $\hat{y}(t)$; and \hat{B}_0 signal of the beam) at the injector output, the collimator output, and after beam transport and acceleration to 20 MeV. The collimator, which limits current by acting as an emittance filter, transmits a portion of the beam pulse which only minimally develops transverse motion of the beam centroid.

Fig. 12. Beam characteristics (I , \bar{x} , \bar{y} , and \hat{B}_0) for beams transported and accelerated through the entire accelerator to full energy. Two sizes of collimators were used, the normal 4 cm diameter and then a 6 cm diameter collimator. The smaller collimator injected 2 kA into the accelerator with no subsequent current loss; the larger collimator injected 3.5 kA into the accelerator and there resulted an ~1 kA distributed current loss throughout the accelerator and reappearance of substantial transverse centroid motion. Both experiments were conducted with identical injector configurations (3 cm cathode-grid gap, grip masked to 250 cm² extraction area and using a 50% transmissive grid mesh).

Fig. 13. With a "wire zone" installed at the 5 MeV location, the beam is injected into the remaining accelerator structure both on center and forward directed. For a range of current values as prescribed by the variable attenuator, the beam centroid is seen to remain within 1 cm of axis, but a distributed current loss still occurs. The graphs show the results of one experiment conducted with a 6-1/2 kA beam current. For all graphs, the horizontal axis represents the number of accelerator cores through which the beam propagated (i.e., z-distance, 200 cores is equivalent to 80 meters accelerator length). Top: peak centroid x-offset, cm; Middle: peak centroid y-offset, cm; Bottom: beam current, kA.

Fig. 1.

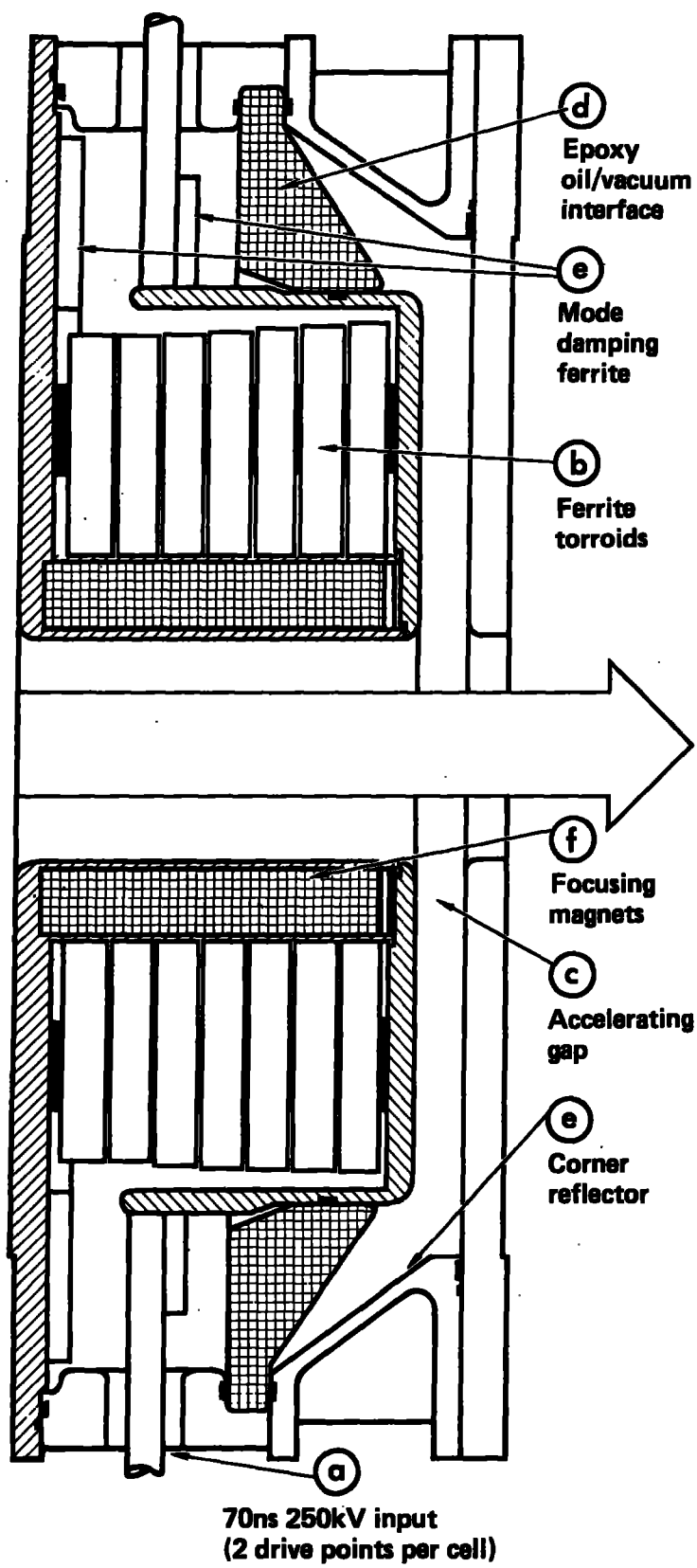
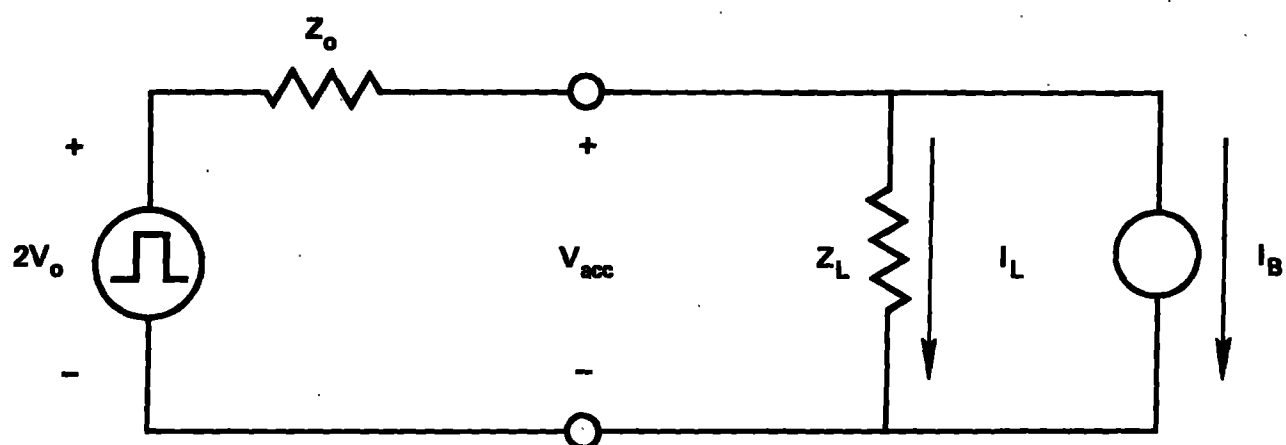


Fig. 2.



$V_o = 250 \text{ kV}$
 $Z_o = 8.3 \Omega$

Nominal design point :

$V_{acc} = 250 \text{ kV}$

$I_B = 10 \text{ kA}$

$I_L = 20 \text{ kA}, Z_L = 12.5 \Omega$

Note: beam is a constant current source, not a resistive or inductive load.

Fig. 3.

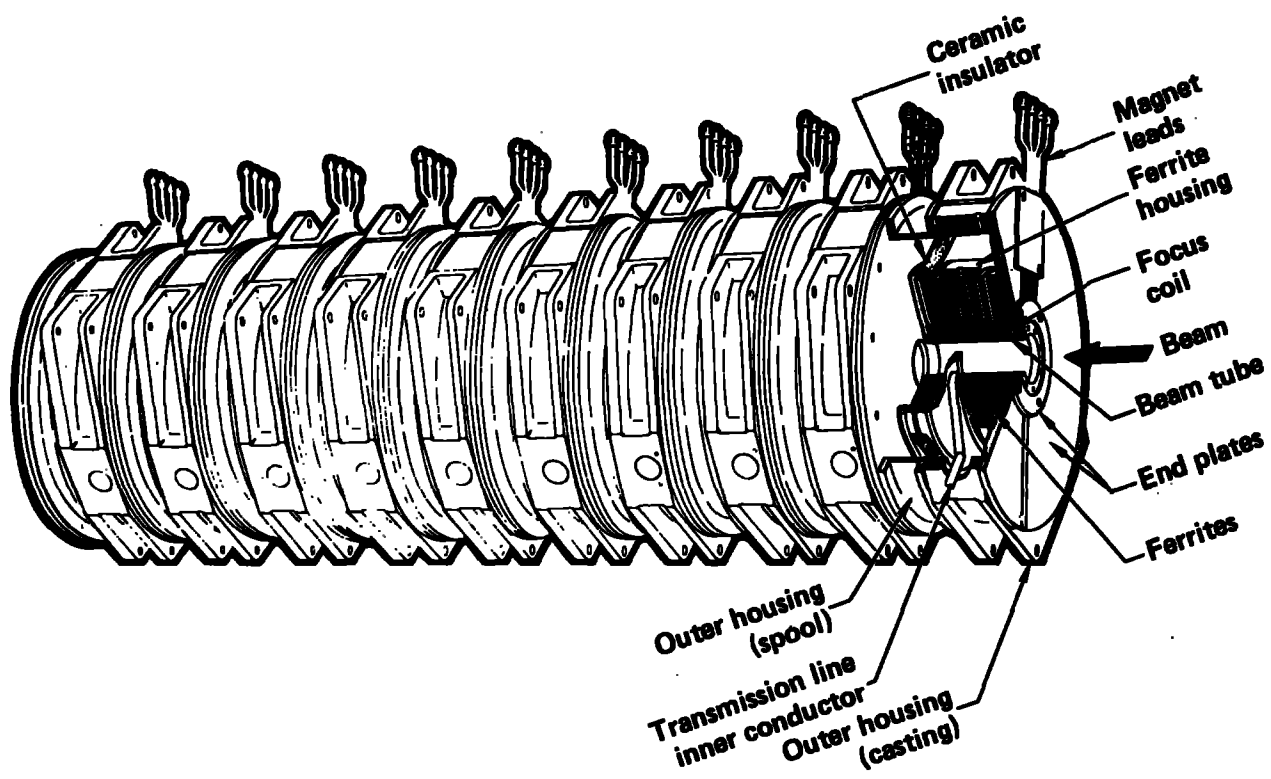


Fig. 4a.

Beam Characteristics

Top photo: current

1 KA/div = 100 mv/div
10 ns/div

X-ray signal emanating from
vacuum wall indicating time
dependent beam spilling onto
wall (relative units, 10 ns/div)

Bottom photo: beam centroid
X(top) Y (bottom)
displacement.

100 mv/div
10 ns/div

Injected into
accelerator

After 10 MeV acceleration
(40 cores)

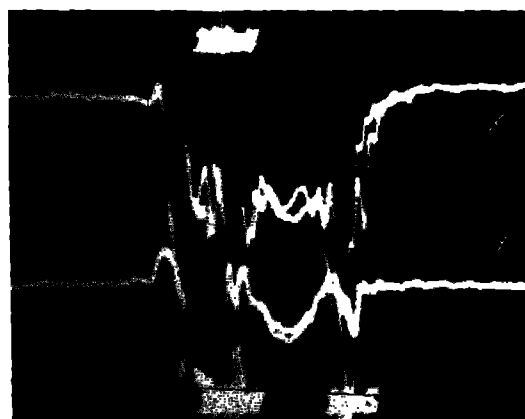
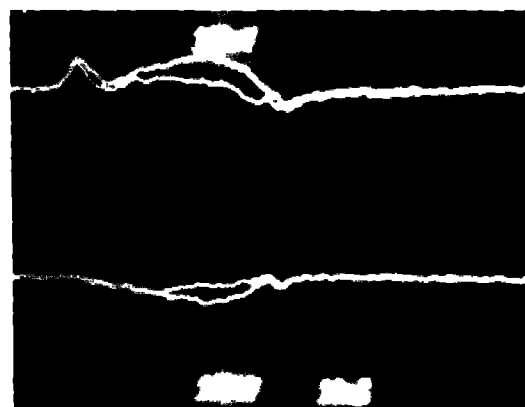
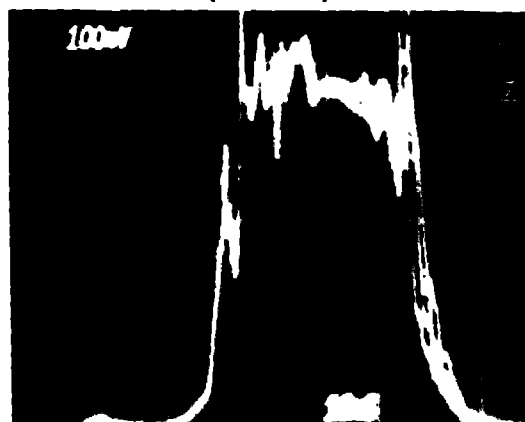
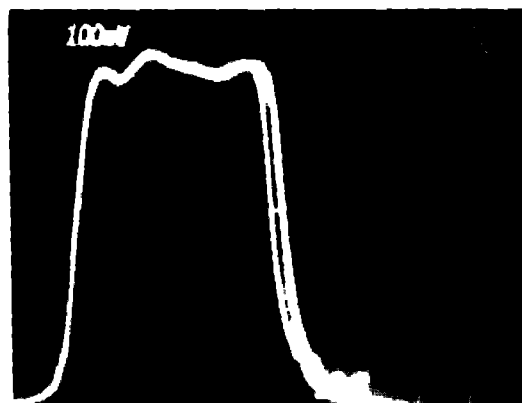
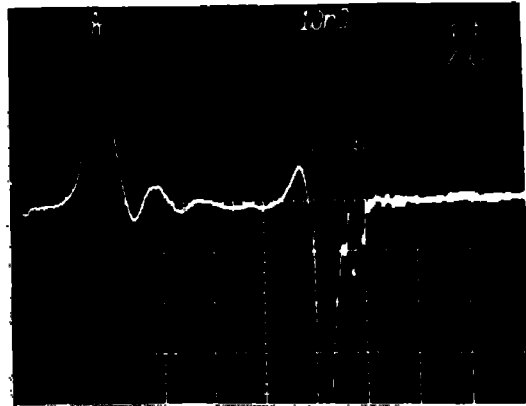
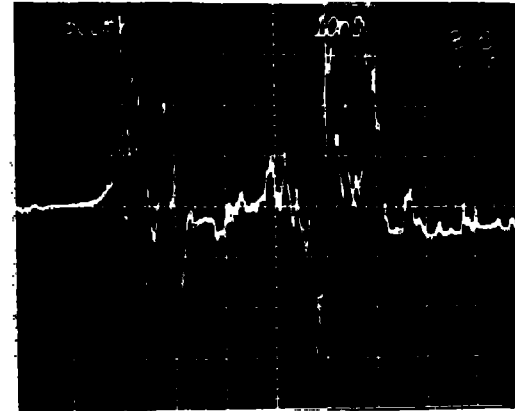


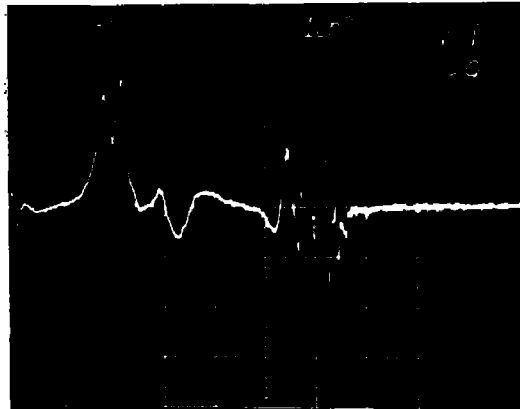
Fig. 4b.



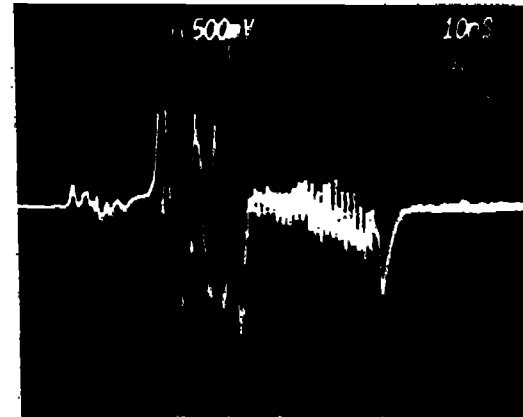
● B_θ @ 2.5 MeV
(beginning of accelerator)



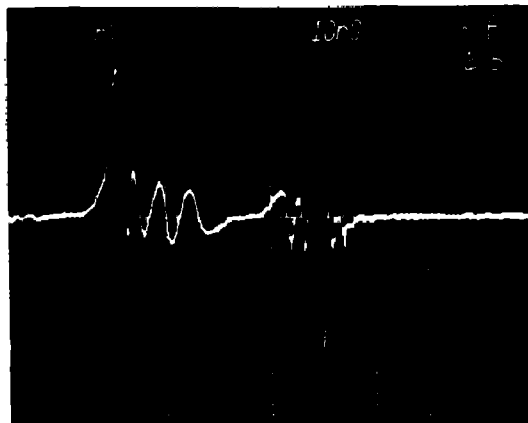
● B_θ @ 8 3/4 MeV
(35 accelerator cores)



● B_θ @ 5 MeV
(20 accelerator cores)



● B_θ @ 10 MeV
(40 accelerator cores)



● B_θ @ 6 1/4 MeV
(25 accelerator cores)

Propagation Characteristics of Slow Rise-Time Beams

At accelerator injection

Top: current 1 kA/div (100 mv/div)
10 ns/div

Bottom: Centroid displacement 100 mv/div
X (top), Y (bottom) 10 ns/div

After 10 MeV accelerator
Same scales

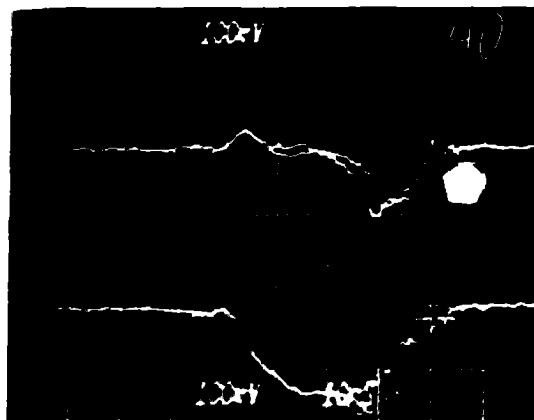
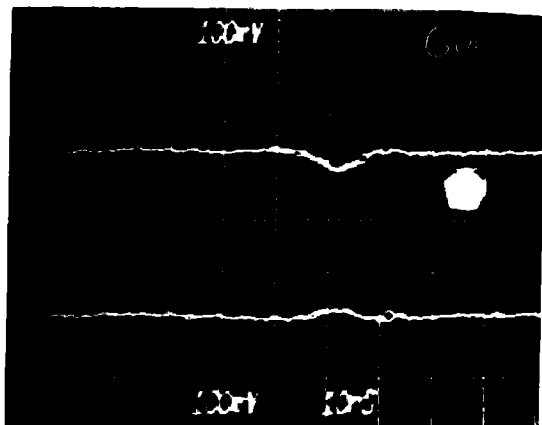
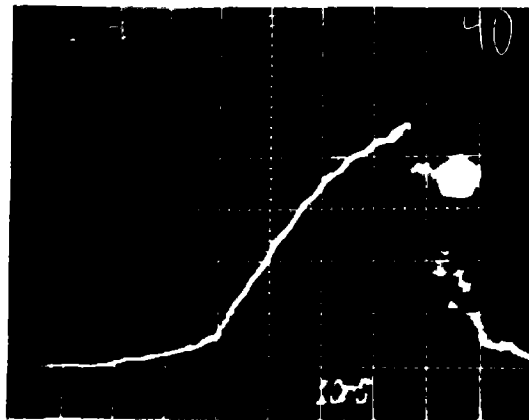
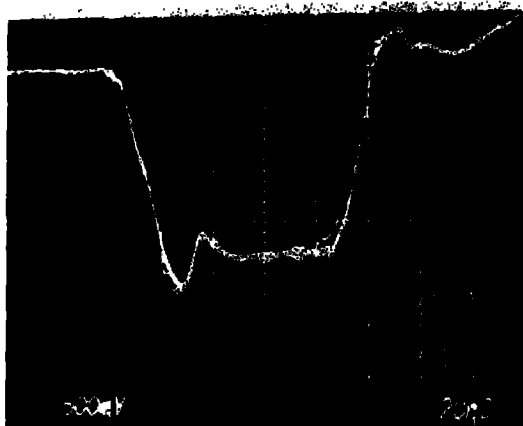


Fig. 5b.

Accelerator core voltage with fast current
rise time (like Fig. 4)

60 kV/div
20 ns/div



Accelerator core voltage with slow
current rise time (like Fig. 5)

60 kV/div
20 ns/div

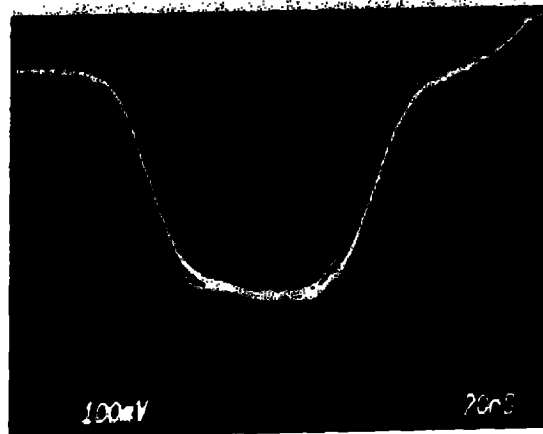
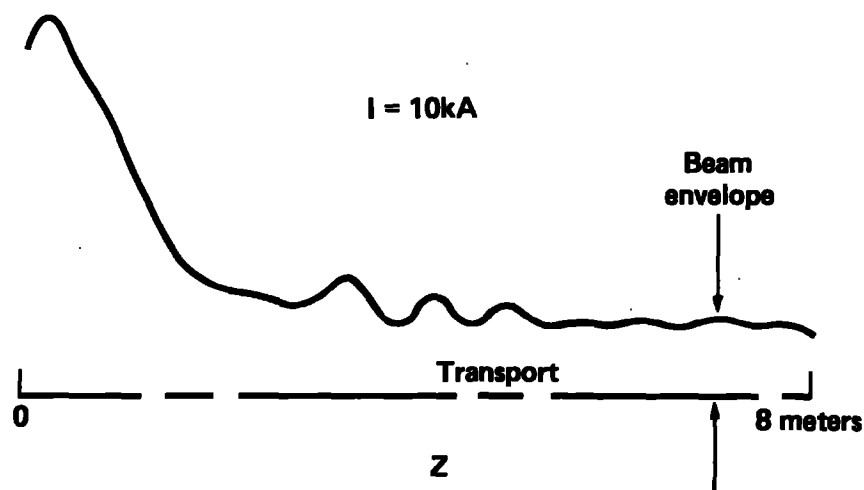
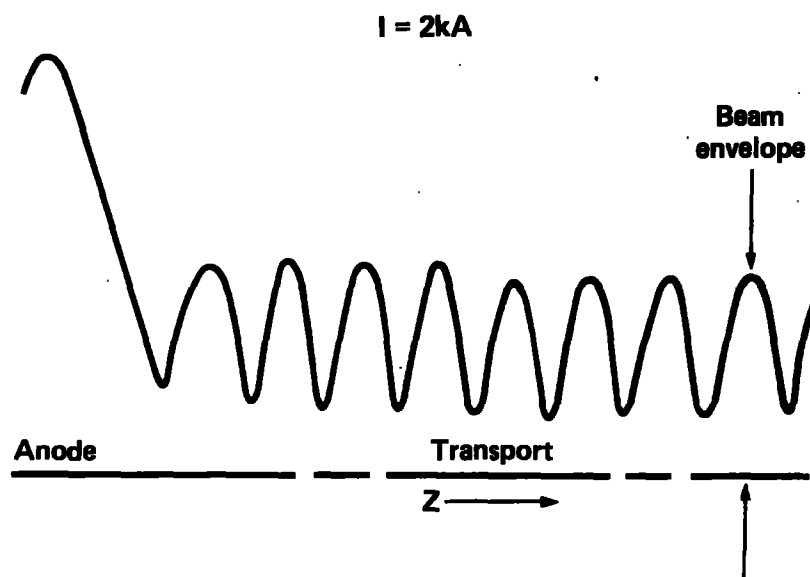


Fig. 6.



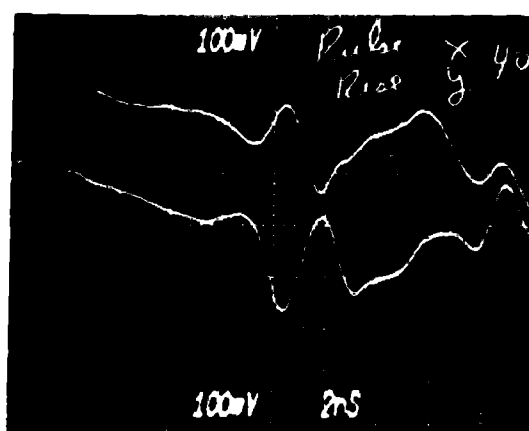
Computed beam envelope for realistic $B_z(z)$ matched (tuned) for minimum oscillators of a 10kA beam current



Computed beam envelope for same $B(z)$ but 2kA beam current (i.e. during current rise time)

Fig. 7.

Top X centroid motion
Bottom Y centroid motion



Beam Characteristics

At accelerator input
Top photo: current 2 kA/div (200mv/div)
10 ns/div

After 10 meV (40 accelerator cores)

Same scales

Bottom photo: Beam centroid displacement 200 mv/div
10 ns/div

Top X displacement
Bottom Y displacement

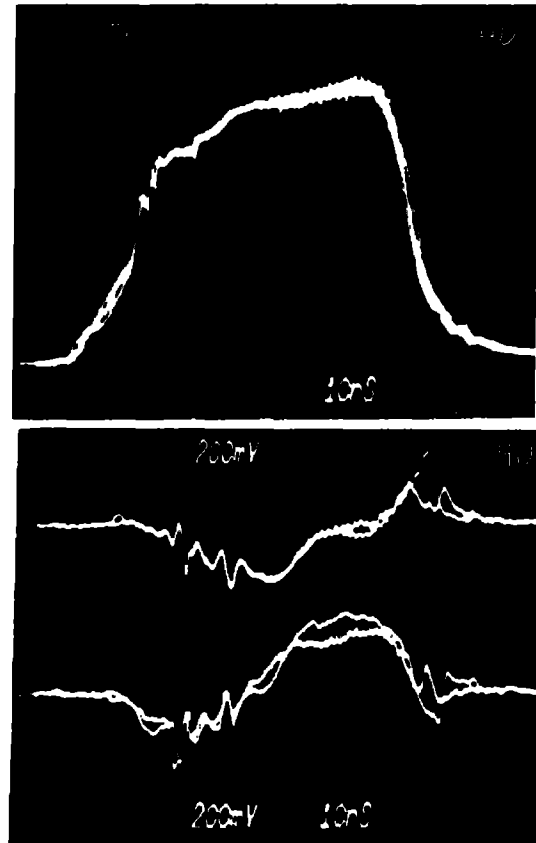
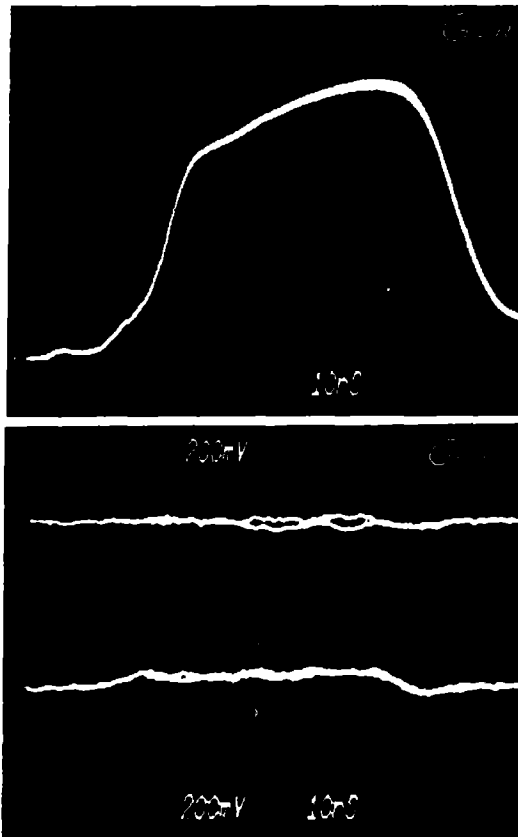
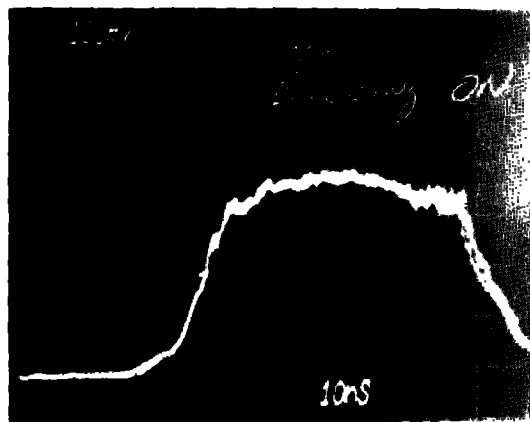
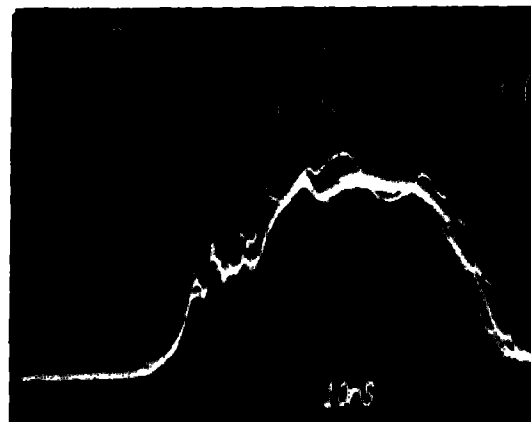


Fig. 9.

All traces are beam current at the 10 MeV location:

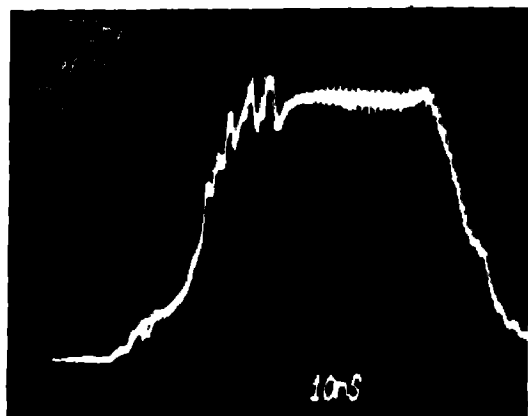


Bucking coil on

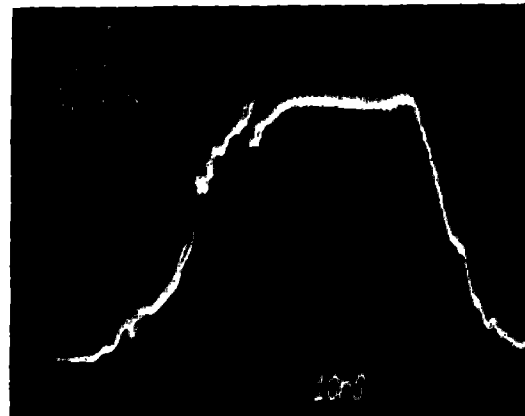


Bucking coil off

Scale 1 kA/div
10 ns/div



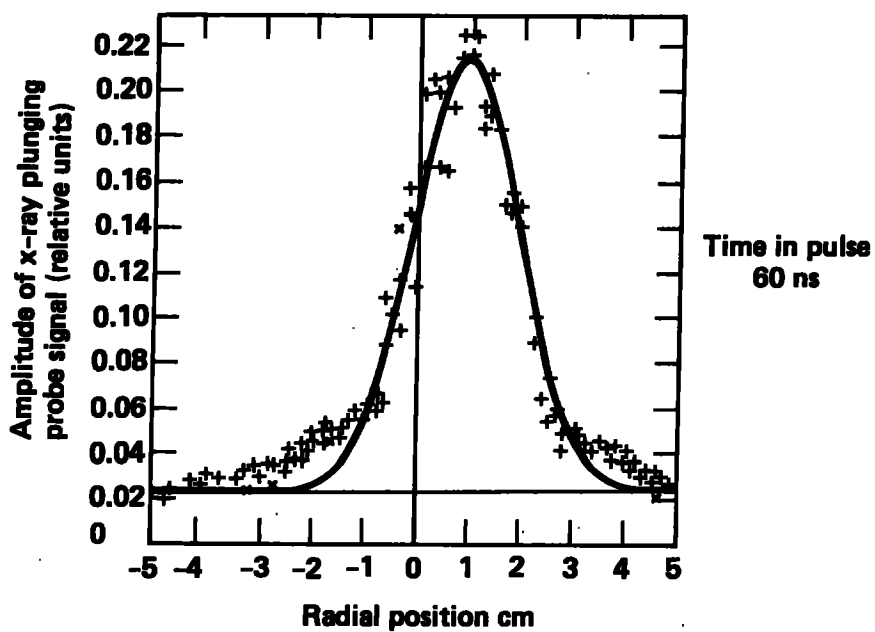
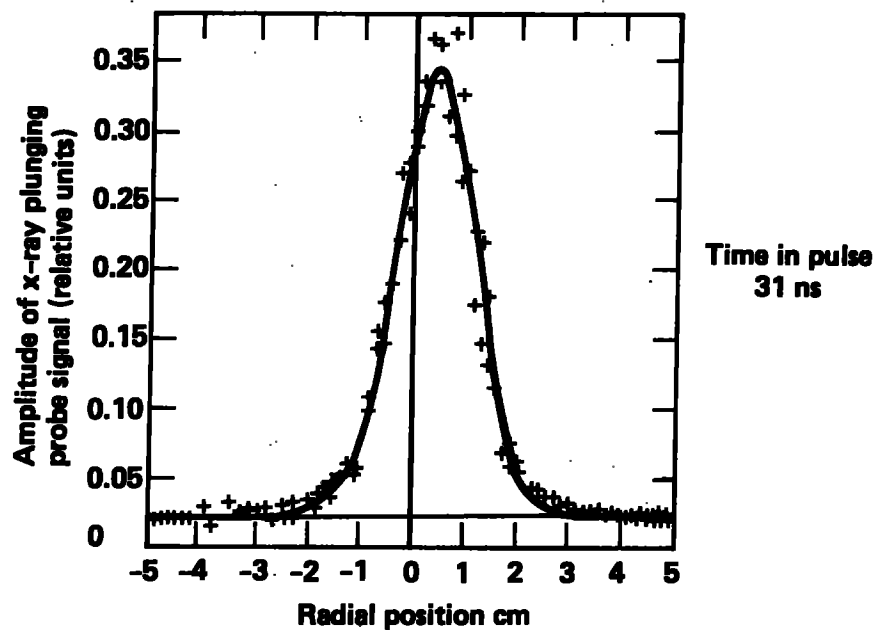
Ignitor timing
80 ns before
grid



Ignitor timing
60 ns before
grid

Scale 2 kA/div
10 ns/div

Fig. 10.



Beam characteristics at
injector output

Beam characteristic at
collimator output

Beam characteristics at 20.0 MeV
(transport through 80 accelerator cores)

Fig. 11.

Top current 1 kA/div (100 mv/div),
10 ns/div
Middle Beam centroid displacement
Top X displacement
Bottom Y displacement
Bottom Beam's B_θ 100 mv/div, 10 ns/div

Top current 0.5 kA/div (50 mv/div),
10 ns/div
Middle Beam centroid displacement
Top X displacement
Bottom Y displacement
Bottom Beam B_θ 200 mv/div, 10 ns/div

Top current 0.5 kA/div (50 mv/div),
10 ns
Middle Beam centroid displacement
Top X displacement
Bottom Y displacement
Bottom Beam B_θ 50 mv/div, 10 ns/div

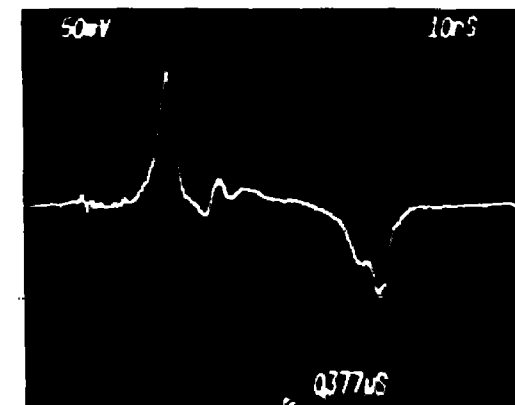
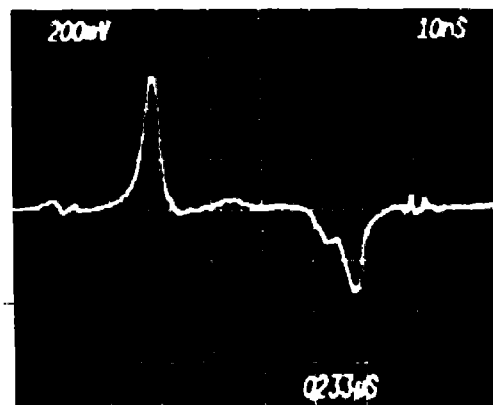
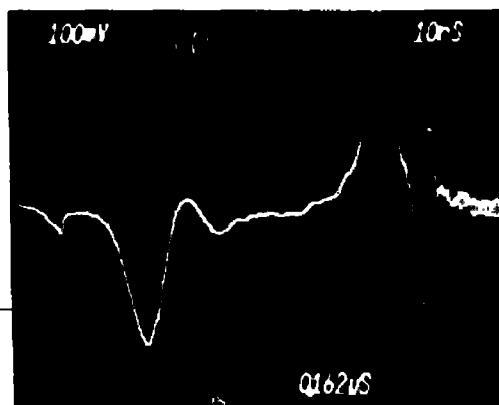
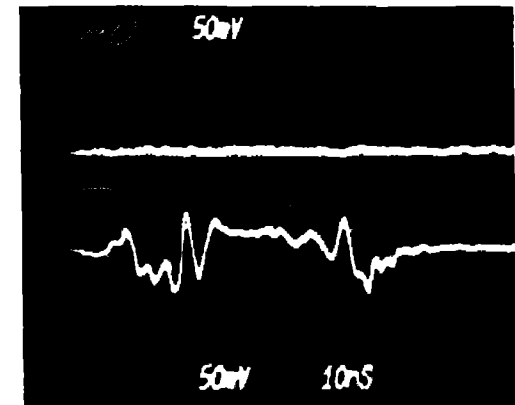
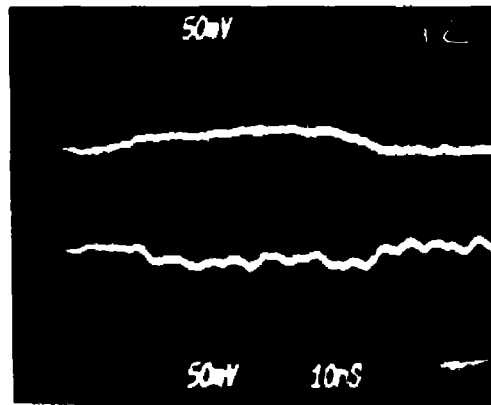
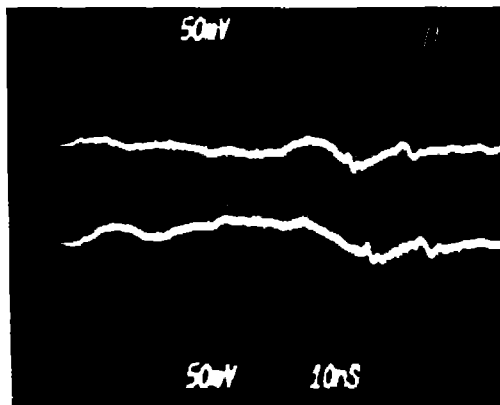
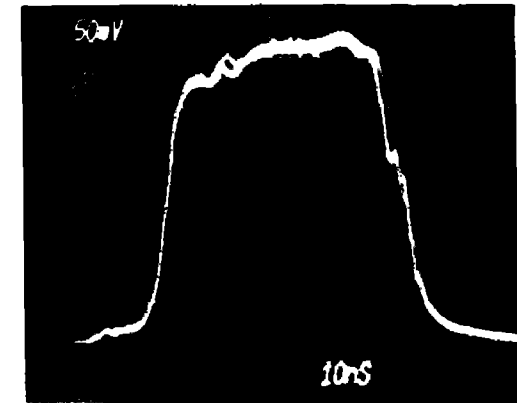


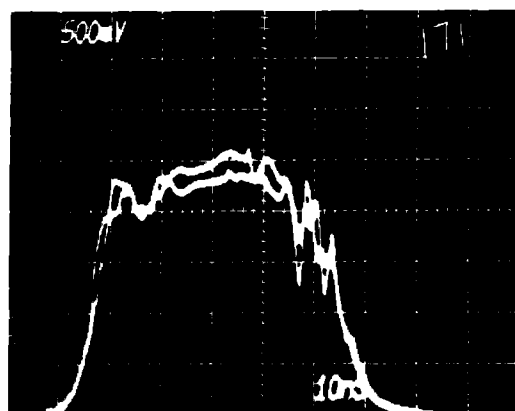
Fig. 12.

Beam characteristics at ~ 45 MeV
(after 180 accelerator cores) but with
6 cm dia (1.06 cm long) collimator
between injector and accelerator

Top: current 0.5 kA/div (50 mv/div 10 ns/div)

Middle: Beam centroid
displacement
(500 mv/div) 10 ns/div
Top X displacement
Bottom Y displacement

Bottom: beam's B_θ 200 mv/div



Beam characteristics at ~ 45 MeV (after 180
accelerator cores) but with 4 cm dia
(1.06 cm long) collimator between
injector and accelerator

Top: current 0.5 kA/div (50 mv/div ns/div)

Middle: Beam centroid
displacement
50 mv/div 10 ns/div
Top X displacement
Bottom Y displacement

Bottom: beam's B_θ 100 mv/div 10 ns/div

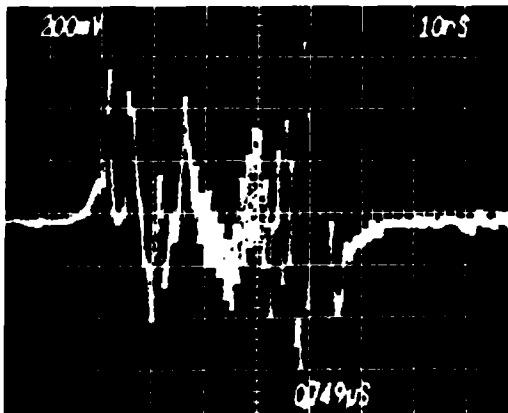
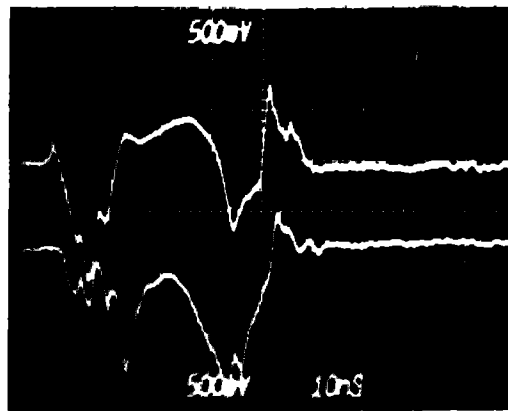
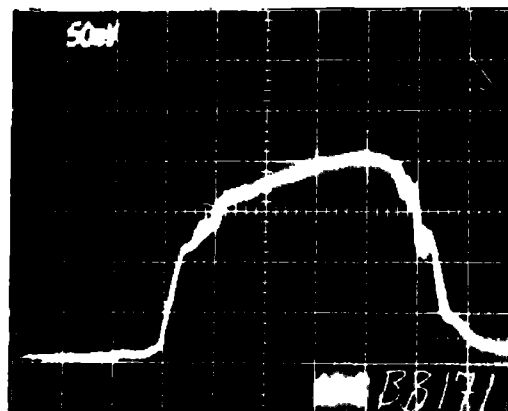


Fig. 13.

